ARTICLE

BIOTECHNOLOGY and BIOENGINEERING

The Effect of Biofilm Permeability on Bio-Clogging of Porous Media

Thomas R.R. Pintelon,[1] Cristian Picioreanu,[2] Mark C.M. van Loosdrecht,[2] Michael L. Johns[3]

[1]Department of Chemical Engineering and Biotechnology, University of Cambridge, Cambridge, UK

[2]Department of Biotechnology, Delft University of Technology, Delft, The Netherlands

[3]School of Mechanical and Chemical Engineering, University of Western Australia, 35 Stirling Highway, Crawley, Western Australia 6009, Australia; telephone: +61-8-64885664; e-mail: michael.johns@uwa.edu.au

Received 30 August 2011; revision received 7 November 2011; accepted 11 November 2011

Published online 17 November 2011 in Wiley Online Library (wileyonlinelibrary.com). DOI 10.1002/bit.24381

ABSTRACT: A 3D Biofilm model, appropriate for complex porous media support structures, is successfully modified such that non-zero permeability of biofilms structures is enabled. A systematic study is then conducted into the influence of biofilm permeability on overall biomass growth rate. This reveals a significant influence at large biofilm concentrations; even when the permeability of the biomass is 1.25% of that of the free pore space, biomass accumulation increased by a factor of ~3 over 40 h. The effect is shown to be retained when allowing for biomass detachment or erosion as a consequence of adjacent velocity shear. We conclude that biofilm permeability should be included in biofilm models and that further experimental work is required to better describe the link between biofilm permeability and local microstructure.

Biotechnol. Bioeng. 2012;109: 1031–1042.

KEYWORDS: 3D biofilm growth model; biofilm permeability; porous media; bio-clogging

Introduction

Biofilms are microbial assemblies that typically form in aqueous environments when microorganisms (e.g., bacteria) attach to an interface through van der Waals forces or cell adhesion structures such as pili (Pratt and Kolter, 1998). During growth, the cells comprising the biofilm excrete extracellular polymeric substances (EPS) whose primary function is to increase the cohesive strength of the biofilm (Lappin-Scott and Costerton, 2003). The EPS mainly consist of polysaccharides, proteins, and DNA, collectively forming a slimy, gel-type layer (Flemming and Wingender, 2002). Besides its ability to hold cells together, the EPS matrix serves as a nutrient reservoir, protects the cells against predator cells, detergents and antibiotics (in some cases antibiotic resistance can be increased 1,000-fold compared to planktonic (i.e., free-floating) bacteria of the same species (Stewart and Costerton, 2001), and facilitates communication among cells through biochemical quorum sensing signals (Fuqua et al., 1994).

Biofilms have proven to be efficient in the formation of bio-barriers to control subsurface contamination plumes (Kao et al., 2001). The main goal of the biofilm in this context is often to reduce the permeability of the subsurface environment and hence effect containment of such plumes. Compared to physical containment methods (e.g., sheet piles) or chemical technology (e.g., permeable reactive walls) bio-barriers often demonstrate increased lifetimes (Kim et al., 2006), whilst also providing contaminant degradation capability. Komlos et al. (2004), for example, extended conventional bio-barrier applicability by creating a field-scale bio-barrier consisting of *K. oxytoca* (permeability reduction) and *B. cepacia* (TCE degradation) bacteria that not only controls TCE contaminant spread but also biologically degraded it. To create bio-barriers, microorganisms are selectively injected into the subsurface or soil, together with appropriate nutrients (Kim et al., 2006). Some cells attach to the soil surface and consequently form biofilms. The injection of bacteria and nutrients into the porous subsurface is probably the most crucial step in the bio-barrier formation process. Shaw et al. (1985) demonstrated that this injection process often causes premature clogging near the injection zone, limiting both bacterial and nutrient transportation lengths. One way to circumvent this problem is the use of starved cells (Macleod et al., 1988), which can consequently be resuscitated (Cunningham et al.,

Correspondence to: M.L. Johns

2003). Cunningham et al. (2003) used this technique and observed reductions in hydraulic conductivities larger than 99% for a 56 m biobarrier, which was maintained over a 2-year period with little supplemental nutrient provision. An improved mechanistic understanding of bio-barrier formation, and ultimately possibly a predictive capacity, will require the development of appropriate biofilm simulation models that are compatible with the complex support structure provided by porous media.

A significant assumption in most existing biofilm simulation models is that biofilm-occupied regions are impermeable and that nutrient provision within the biofilm is purely as a result of diffusion. However, experimental studies have demonstrated that biofilm morphology is often extremely heterogeneous and can contain voids (e.g., Flemming et al., 2000). As a result, biofilms are not fully impermeable and can contain a significant amount of both *static* and *dynamic* water (Flemming et al., 2000). In the absence of biofilm detachment, the effect of permeability is only relevant when biofilm growth is nutrient mass transfer limited. Such conditions are prominent in subsurface conditions (Kim and Fogler, 2000) and are very relevant to bio-barrier scenarios where thick biofilms are desirable for permeability reduction.

We have developed a 3D biofilm model applicable to random porous media (Graf von der Schulenburg et al., 2009) based on lattice Boltzmann (LB) simulation methods for pore-scale hydrodynamics and solute diffusion in the resultant flow-field. In Pintelon et al. (2009), we extended this modeling platform to allow for a consideration of biofilm detachment in response to the adjacent velocity shear field and subsequently explored the most energy-efficient way of establishing and maintaining a bio-barrier. Both of these publications however treated the biofilm regions as being impermeable. In the current article we extend this biofilm modeling platform to allow for a permeable biofilm, with different permeability being possible for the free pore-space and biofilm-occupied pore-space of the porous medium, respectively. We proceed to explore the effect of the relative magnitude of this biofilm permeability on biofilm growth rate, both with and without biofilm detachment due to adjacent shear rates. In this manner we hope to enable a decision on what conditions require a consideration of biofilm permeability in relevant modeling platforms and help direct experimental efforts to make this inclusion more realistic.

Background

A variety of 2D and 3D biofilm growth models have been developed and reported in the literature [a relatively recent overview is given by Wanner et al. (2006)]. These have been successfully applied to a range of industrial scenarios ranging from biofouling of reverse osmosis membranes (Radu et al., 2010) to mineral ore bioleaching (Olivera-Nappa et al., 2010). In terms of their application to bio-barriers, or more generally porous media, Clement et al., (1997) and Taylor et al. (2002) considered a bio-barrier simulation model assuming homogeneous biofilm growth on soil particles. Resolving the pore space of the host porous media, Vandevivere and Baveye (1992) first proposed a one-dimensional pore network model; a two-dimensional pore network model was subsequently introduced by Thullner et al. (2002). They both assumed that microbial colonies preferably blocked pores of particular sizes, and that biomass was impermeable to flow. These models, and most other biofilm models reported in the literature assume impermeable biofilms, hence that nutrient transport occurs through the biofilm only by molecular diffusion.

Kapellos et al. (2007) included biofilm permeability within 2D biofilm simulations using a closed analytical solution to the creeping flow of an incompressible, Newtonian fluid based on the effective medium (EM) concept. In this EM method, heterogeneous biofilm is represented by a unit cell embedded in an effective porous medium. The unit cell model distinguishes between different constituents: (i) Biological cells (assumed to be impermeable with smooth surface), (ii) hydrated(EPS) and EPS fibres, and (iii) aqueous solution not bound in the EPS matrix. The effective permeability of the biofilm is then calculated from the analytical solution of creeping flow for each unit cell. This permeability value was then used in the overall momentum balance which was solved numerically. The resulting permeability distribution is thus a complex function of geometrical and physicochemical properties. Thullner and Baveye (2008) included flow through permeable biofilms in their pore network model, assuming that water has a different viscosity in the biofilm than in the open space; this approach was suggested by Dupin et al. (2001a, b). More specifically, the assumption is that the viscosity of the liquid phase flowing through the biofilm, μ_b, is given by:

$$\mu_b = X \cdot \mu \tag{1}$$

with μ the actual dynamic viscosity of the fluid. When $X = \infty$, the biofilm is impermeable, whereas the case with $X = 1$ corresponds to a biofilm that offers no additional resistance to water flow. Thullner and Baveye (2008) used values of $X = 10^9$ (tagged as *impermeable* biofilm) and 10^3 (*permeable* biofilm) in their simulation studies. Assuming that the biofilm structure is a porous medium, biofilm permeability, κ_{bio}, can be expressed using Darcy's law:

$$\mathbf{u} = \frac{\kappa_{bio} \nabla p}{\mu L} \tag{2}$$

where $\mathbf{u}$ is the fluid flow velocity through the biofilm, L the length of the biofilm and $\bigtriangledown p$ the pressure drop over the biofilm. The artificial effect of increasing viscosity is actually to reduce permeability for an actual constant viscosity. Using this approach Thullner and Baveye (2008) were able to simulate comparatively larger reductions of the overall

hydraulic conductivity of the pore networks, similar to those obtained in laboratory experiments and observed in field situations.

Model Description and Development

Because of the spatial heterogeneity of both biofilms and the support structure provided by typical porous media, 3D modeling is very desirable. In the current work we utilize the LB method to simulate both hydrodynamics and solute mass transfer within a 3D porous media at the pore-scale. LB methods have been shown to be able to accurately simulate flow and diffusion in complex geometries such as porous media (e.g., Freund et al., 2003; Raabe, 2004; Zeiser et al., 2001) and have been accurately validated using experimental magnetic resonance imaging (MRI) data (e.g., Maier et al., 1998; Manz et al., 1999; Sullivan et al., 2006).

The inclusion of biofilm permeability into our biofilm modeling platform has the following implications:

(i) Nutrient supply to the biocells within the biofilm is no longer determined only by diffusion but also by advection through the biofilm gel, resulting in an increase in biofilm growth kinetics. This of course assumes that the system is mass transfer limited.
(ii) Comparative shear stresses on the surface of biofilms decrease, resulting in less biomass detachment provided appropriate biofilm yield stresses are exceeded.

Existing Biofilm Growth Model

The LB simulation method was used to solve the Navier–Stokes continuity equations for the conservation of mass (Eq. 3) and linear momentum (Eq. 4), which describe the hydrodynamics through the porous medium.

$$\nabla \cdot \mathbf{u} = 0 \tag{3}$$

$$\frac{\partial \mathbf{u}}{\partial t} + \mathbf{u} \cdot \nabla \mathbf{u} = -\frac{1}{\rho}\nabla p + \nu \nabla^2 \mathbf{u}, \tag{4}$$

where $\mathbf{u}$ is the velocity vector, t is time, p is pressure, ρ is density, and ν is kinematic viscosity. The LB hydrodynamics method was implemented in 3D using 19 velocity directions (known as D3Q19) and using the multiple relaxation time (MRT) LB variant (d'Humières et al., 2002). Compared to the more conventional Bhatnagar–Gross–Krook (LBGK) method, MRT presents superior numerical stability allowing faster, more relevant, flow rates to be simulated. To attain an optimized stability of the LB model, optimal MRT relaxation parameters as reported in Lallemand and Luo (2000) were used, which were obtained through systematic linear analysis of the generalized hydrodynamics of the model. The mass transport LB method used here is based on the model proposed by Flekkøy (1993) on a 3D 7 velocity (D3Q7) lattice and solves the advection-diffusion-reaction equation:

$$\frac{\partial C_s}{\partial t} + \mathbf{u} \cdot \nabla C_s - D_s \nabla^2 C_s = r_s \tag{5}$$

where C_s is the nutrient concentration, D_s is its diffusion coefficient, and r_s is it local consumption rate. Biofilm growth is described using an individual-based biofilm growth model (IbM); this was developed by Picioreanu et al. (2000) and Kreft et al. (1998). In this approach biocells are not required to be discretized on the grid used by the LB models. The IbM simulation is coupled to the LB description of flow and resultant nutrient concentration fields. The local nutrient consumption rate, r_N, is quantified according to Monod kinetics (Beeftink et al., 1990):

$$r_N = -q_{max} C_X \frac{C_N}{K_N + C_N}, \tag{6}$$

where C_X and C_N are the local biomass and nutrient concentrations, K_N is the Monod half saturation coefficient and q_{max} is the maximum specific uptake rate. The growth rate of biomass is then described by Equation 7, with Y_{XN} the yield stoichiometric coefficient of the nutrient.

$$\frac{dC_X}{dt} = -Y_{XN} r_N \tag{7}$$

Biomass growth results in a reduction of available pore space for flow and thus a revision of the LB simulated flow field. Although the LB method is based on a discrete grid, the individual-based biofilm model uses continuous Cartesian space in 3D to describe the different biofilm proliferation steps. The resultant simulation algorithm is shown in Figure 1; more detailed discussion and explanation is contained in Graf von der Schulenburg et al. (2009) and the inclusion of shear induced biofilm detachment using the level set method is described in more detail in Pintelon et al. (2009). The extent of biomass detachment (erosion) is defined by the detachment level set (DLS) parameter, which defines the value of the level set front, φ, until where biomass is allowed to detach. This DLS value was given a physical meaning by correlating it with the erosion velocity per unit velocity shear stress adjacent to the biofilm. We acknowledge that this is a relatively simple approach relative to that presented by Klapper et al. (2002) and Alpkvist and Klapper (2007), who treat the biofilm as a viscoelastic fluids, future work will focus on implementing this more rigorous description of biofilm strength. "Inoculation" of the bacteria, at time 0, that adhere to the porous medium and produce viable proliferating biofilm colonies, is an effectively random process dictated by numerous factors. Here we simulate this adherence process using a directed random walk (DRW) algorithm, further details are available in Pintelon et al. (2010). Experimental validation of this

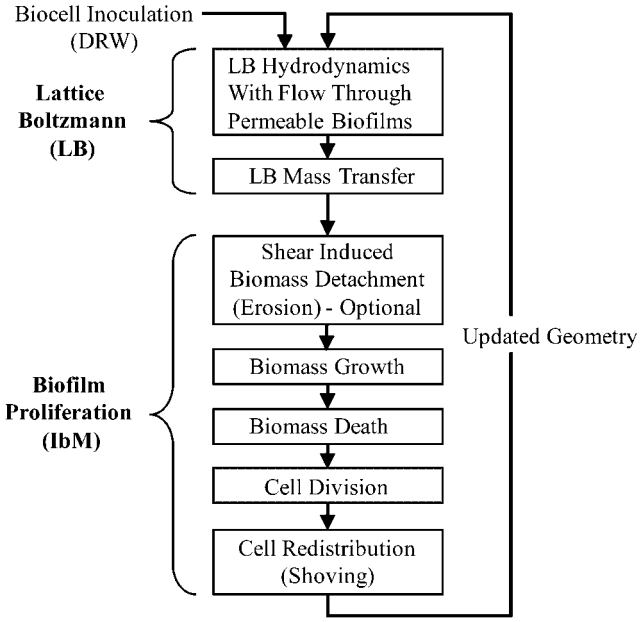

Figure 1. Biofilm growth algorithm used.

existing biofilm modeling approach was also conducted in Pintelon et al. (2010) via quantitative 3D comparison with MRI images of biomass accumulation on membrane systems.

Method Development—Inclusion of Biofilm Permeability

d'Humières et al. (2002) demonstrated that the MRT LB relaxation rates s_9^{-1} and s_{13}^{-1} determine the LB kinematic viscosity, ν, in the same way as the LBGK relaxation parameter τ in the Single Relaxation Time (SRT) LB method:

$$\nu = \frac{1}{3}\left(\tau - \frac{1}{2}\right) \tag{8}$$

In this work, we chose s_9 and s_{13} to be equal to τ^{-1}, hence the kinematic viscosity, ν, of the fluid flow simulated with the MRT LB method also obeys Equation 8. Below, we explain the inclusion of biofilm permeability by manipulation of the LB relaxation parameter τ. As τ defines SRT and MRT viscosity in the same way, the proposed method extension is both valid for SRT and MRT LB. Within biofilm-occupied simulation lattice nodes, we define the LB relaxation parameter for flow, τ_b:

$$\tau_b = n_b \cdot \tau, \quad n_b > 1 \tag{9}$$

The parameter n_b can be denoted as a biofilm impermeability factor. Combining Equations 2,8 and 9 gives the biofilm apparent viscosity as:

$$\nu_b = \frac{1}{3}\left(\tau_b - \frac{1}{2}\right) = \frac{1}{3}\left(n_b \cdot \tau - \frac{1}{2}\right) = \frac{\kappa_{bio} \cdot A \cdot \Delta p}{\rho \cdot Q \cdot L}, \quad n_b > 1 \tag{10}$$

with ρ the density of the fluid. The kinematic viscosity of fluid streaming through the biofilm, ν_b, is thus proportional to n_b. The ratio of the kinematic viscosities within the biofilm, ν_b, and the free bulk liquid, ν, is given by:

$$\frac{\nu_b}{\nu} = \frac{\mu_b}{\mu} = \frac{\tau_b - 1/2}{\tau - 1/2} = \frac{n_b \cdot \tau - 1/2}{\tau - 1/2} = X \tag{11}$$

with μ_b and μ the respective dynamic viscosities and X is the parameter in Equation 1 introduced by Thullner and Baveye (2008). This pseudo-viscosity for flow within the biofilm aggregate is set higher ($n_b > 1$) than the normal water viscosity to account for increased resistance to flow within the biofilm-occupied region. The use of MRT LB as opposed to SRT LB allows a broader range of X to be explored where numerical stability is retained despite the sudden change in apparent viscosity across the free pore space—biofilm-occupied pore space interface.

Simulations Performed

3D simulations were conducted on a $2{,}400 \times 2{,}400 \times 2{,}400\ \mu m^3$ porous domain discretized on a LB matrix of $120 \times 120 \times 120$ nodes with an isotropic voxel resolution, Δx, of 20 μm and a porosity of 0.5. The matrix including the discretized distribution of solid and liquid in the porous medium was obtained via MRI of a saturated random packing of glass beads. The resulting 3D simulation lattice is shown in Figure 2. The mean size of the spherical beads in the simulation matrix was 400 μm. The constant inlet z velocity (at $z = 0\ \mu m$) was set to $0.02\ mm.s^{-1}$ with a zero pressure boundary defined at the outlet. The nutrient inlet concentration was set to $0.01\ kg.m^{-3}$, which corresponds to the equilibrium concentration of oxygen in water at room temperature and atmospheric pressure (Weiss, 1970), thus oxygen was considered to be the rate-limiting nutrient requirement in all simulations performed here. The diffusion coefficient of oxygen in free water and biofilm was set to $2.0 \times 10^{-10}\ m^2.s^{-1}$. Based on the DRW algorithm, the geometry was inoculated with 29,298 bio-cells with an initial cell mass of 1.0×10^{-14} kg. The duration of each biofilm simulation step was 1.5 h. The minimum and maximum allowed cell masses were 5.0×10^{-15} kg and 20.0×10^{-15} kg (corresponding to cell radii of 4.4 and 7.1 μm). The maximum specific uptake rate, q_{max}, was set to $28\ day^{-1}$ and the Monod half saturation coefficient, K_N, to $5.0 \times 10^{-2}\ kg.m^{-3}$ (see Eq. 6). The yield stoichiometric coefficient, Y_{XN}, of the nutrients was set to $0.5\ kg.kg^{-1}$ (see Eq. 7). These kinetic parameters lie within the range of aerobic biofilm

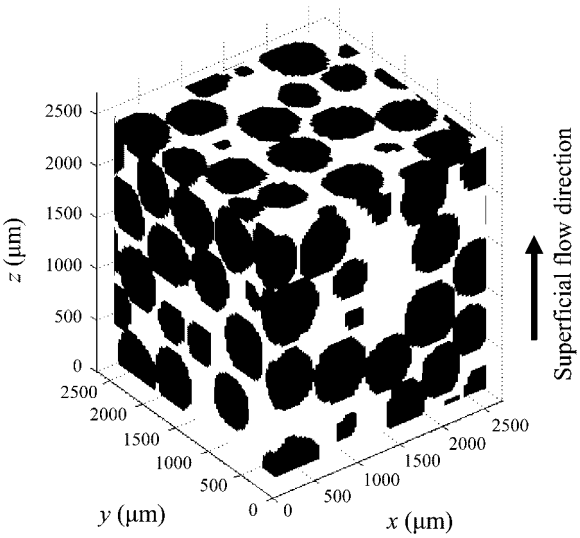

Figure 2. 3D Simulation Lattice. Flow and biomass accumulation occur in the "white" pore space.

growth conditions as reported by Gikas and Livingston (1997); Hu et al. (2005); and Park and Lee (2005).

Simulations were conducted for $X = 3$, 30, 80, and ∞ (impermeable), respectively in the absence of shear-induced biofilm detachment. These were then repeated for biofilm detachment employing average erosion velocities per unit shear, $u_{e,w}$, of 1.7×10^{-9} and 3.5×10^{-9} m.s^{-1}.Pa^{-1}, respectively. Table I presents a summary of the key simulation parameters used.

Results and Discussion

Sample Results and Biomass Accumulation Rates—No Biofilm Detachment

Figure 3 shows the simulated z velocity field at slice $z = 600$ μm after 27 h of biofilm growth for the impermeable biofilm ($X = \infty$) and permeable biofilms with $X = 80$ and $X = 3$, in the absence of biofilm detachment. These 2D slices are extracted from the full 4D simulation data sets for visualization purposes. In Figure 3(a), biofilm accumulation is shown in green; in Figure 3(b) this color coding for biofilm is omitted to enable visibility of the full velocity field, including that within the biofilm-occupied regions. Several features are immediately evident: (i) Greater biomass accumulation is evident with increasing biofilm permeability; (ii) higher velocities are evident in biofilm occupied regions as permeability is increased (this is highlighted in the white box); and (iii) larger velocities are generally evident in the free pore space as permeability is reduced (this is highlighted by the red box). (i) and (ii) are perhaps intuitively obvious, (iii) results from the reduced effective area for flow in the less permeable cases exceeding the effect of a reduced biomass growth rate and hence greater free pore-space for flow. Note that we are considering a constant total volumetric flowrate. Figure 4 shows the nutrient concentration field for the same z-slice as Figure 3, (a) again indicates the location of biofilm whilst (b) excludes the color coding of biofilm. As expected, nutrient concentration within the biofilm is higher as biofilm permeability increases (highlighted by the white boxes).

In Figure 5(a) we show the biomass accumulation ($m_{bio}.V_p^{-1}$) within the lattice as a function of time as extracted from the corresponding 4D data sets. Accumulation rates are virtually identical up to approximately 20 h at which point significant divergence is observed with a very strong dependence on biofilm permeability. This we believe to be a result of the development of sufficiently thick biomass colonies such that nutrient mass transfer limitations are effective; we explore this quantitatively below. What is also obvious is that after 40 h, even a system featuring a biofilm permeability of 1/80 of that of the free space presents a comparative increase in biomass by a factor of 3.08. Figure 5(b) shows the ratio between liquid velocity in the biofilm, u_{bio}, and bulk liquid velocity, u_{bulk}, as a function of biomass accumulation in the system. This ratio increases with biofilm permeability as expected, interestingly for $X = 3$, u_{bio} slightly exceeds bulk liquid velocity, u_{bulk}, after significant biofouling, suggesting that biomass accumulation is preferentially occurring in what were originally fast flowing regions, consistent with the effective activation of mass transfer limitations. Figure 5(c) shows average nutrient concentration within the biofilm, C_N, as a function of biomass accumulation. Higher values are observed for higher permeability biofilms as expected. There is a distinct difference with the impermeable biofilm indicating the role played by advection in nutrient provision to the biofilm internals.

Table I. Simulation parameters

Parameter	Value	Parameter	Value
D	2.0×10^{-10} m^2.s^{-1}	q_{max}	28 day^{-1}
Initial cell mas	1.0×10^{-14} kg	K_N	5.0×10^{-2} kg.m^{-3}
Biofilm simulation step	1.5 h	Y_{XN}	0.5 kg.kg^{-1}
Cell radii (min.)	4.4 μm	X	3, 30, 80, or ∞ (impermeable)
Cell radii (max.)	7.1 μm	$u_{e,w}$	1.7×10^{-9} or 3.5×10^{-9} m.s^{-1}.Pa^{-1}

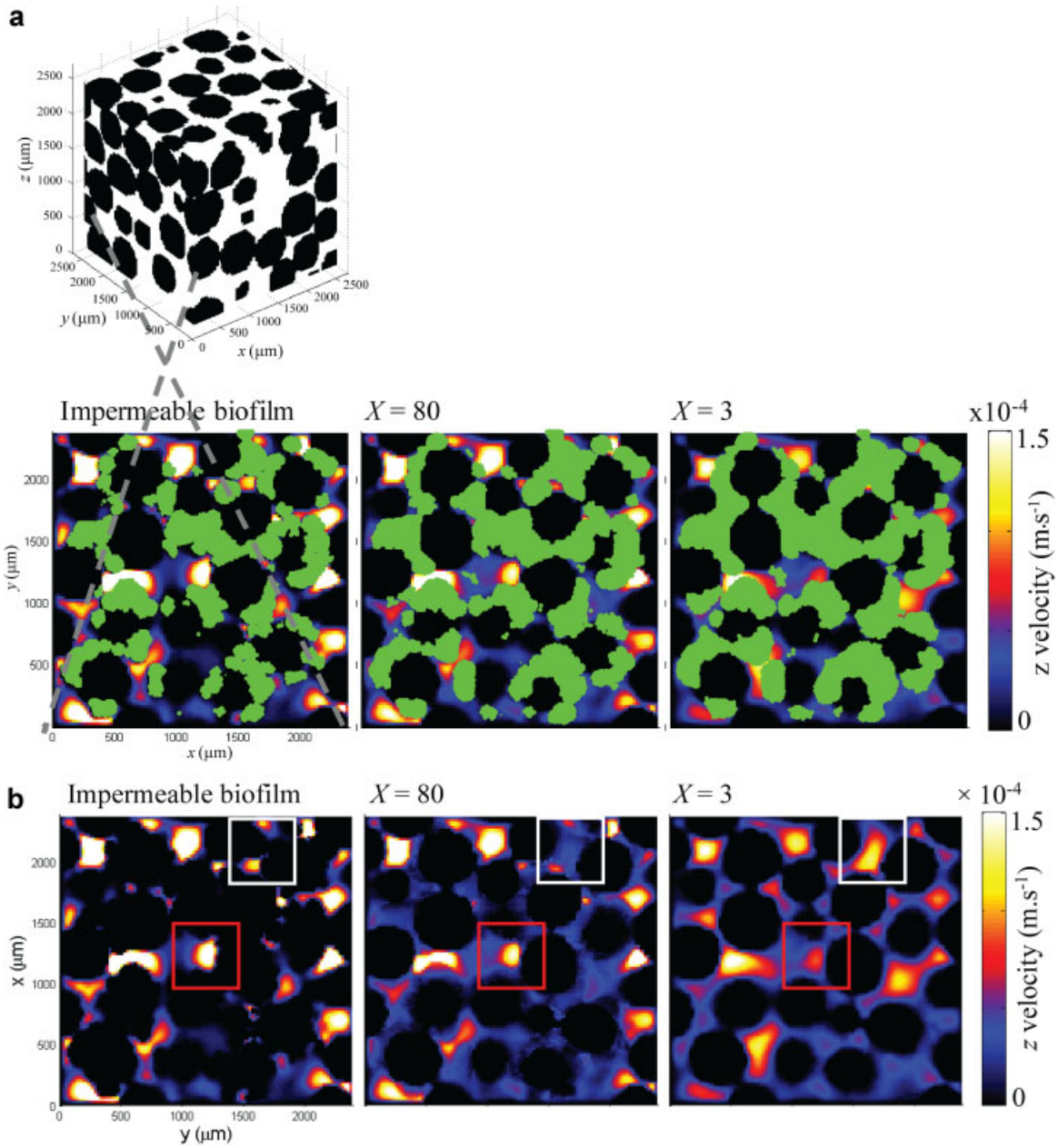

Figure 3. *z* (superficial flow direction) velocity maps at slice $z = 600$ μm (of a full 4D simulation) after 27 h of biofilm growth for an impermeable biofilm and permeable biofilms with $X = 80$ and $X = 3$. Biocells are shown in green (**a**) and were omitted in the second row of images (**b**) to visualize the flow field through the biofilm. [Color figure can be seen in the online version of this article, available at http://wileyonlinelibrary.com/bit]

Dimensionless Group Analysis

Nutrient mass transfer to the biofilm regions is an interplay of diffusion and advection through the biofilm structure. The relative importance of these two mechanisms can be captured by the dimensionless Peclet number (Pe), which is a measure for the ratio between advective and diffusive mass transport:

$$\mathrm{Pe} = \frac{u \cdot h}{D} \tag{12}$$

with h the characteristic length (which we take in this work to be the average biofilm colony height), u the relevant velocity, and D the relevant diffusion coefficient. A distinction can also be made between the internal and external Pe numbers ($\mathrm{Pe_i}$ and $\mathrm{Pe_e}$, respectively) depending on whether u_{bio}, the average fluid velocity in the biofilm, or u_{bulk} the average bulk fluid velocity is used for u. A substantial body of work in the context of mass transfer in porous media, largely in the context of catalyst packings, (e.g., Bijeljic et al., 2004; Sahraoui and Kaviany, 1994) suggests that Pe numbers in excess of 10 would indicate

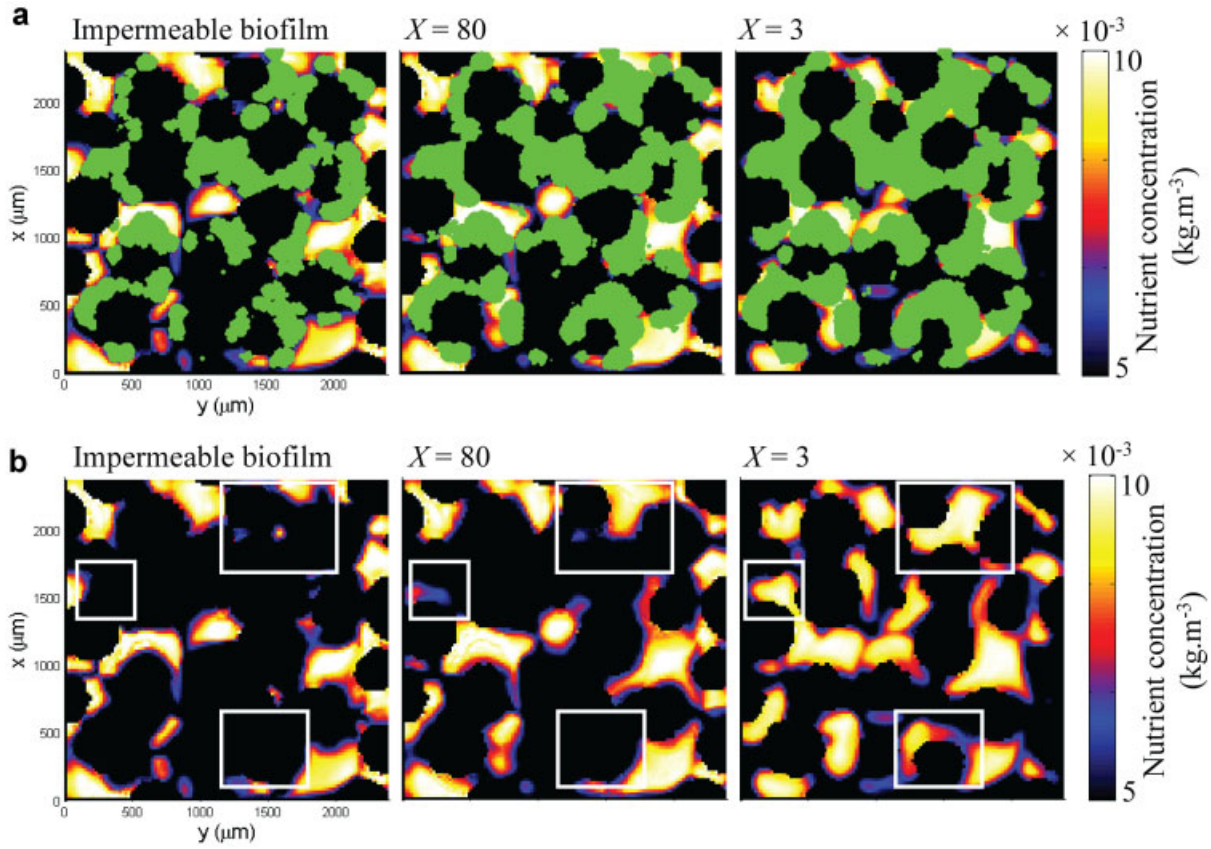

Figure 4. (a) Nutrient concentration at slice $z = 600$ μm (of a full 4D simulation) after 27 h of biofilm growth for an impermeable biofilm and permeable biofilms with $X = 80$ and $X = 3$. (b) Cells were omitted to visualize in the second row of images to visualize the nutrient concentration field within the biofilms. [Color figure can be seen in the online version of this article, available at http://wileyonlinelibrary.com/bit]

dominance by advection. In Figure 6(a) and (b) we plot Pe_i and Pe_e as a function of biomass accumulation. In the case of Pe_e is consistently in excess of 10 whilst Pe_i transitions through 10 during the course of the simulation for all permeable conditions considered [consistent with the divergence observed in Fig. 5(a)]. This analysis can only be considered semi-quantitative given the complex geometry and the different values used across the literature to define L; however it does highlight the importance of advection in our simulations and that perhaps Pe_i is a better indication of this importance. It is acknowledged that Pe_i would be very difficult to determine experimentally.

In terms of the system being mass transfer limited, i.e., the competition between nutrient mass transfer (advection and diffusion) and nutrient consumption, is best captured by the first Damköhler number (Da), which represents the ratio of nutrient consumption to advective supply. Again we distinguish between internal and external Da numbers (Da_i and Da_e, respectively):

$$Da_i = \frac{\tau_r}{\tau_a} = \frac{q_{max} \cdot \frac{C_N}{C_N + K_N}}{\frac{u_{bio}}{h}} \quad (13)$$

$$Da_e = \frac{q_{max} \cdot \frac{C_N}{C_N + K_N}}{\frac{u_{bulk}}{h}} \quad (14)$$

with τ_r and τ_a the characteristic time scales for reaction and advection, respectively, C_N the average nutrient concentration within the biofilm, q_{max} the maximum specific uptake rate, and K_N the Monod half saturation coefficient. For relatively low Da numbers, i.e., when nutrient consumption rates are low compared to nutrient provision, nutrients are almost homogeneously supplied to the different biofilm colonies in the system. For relatively large Da numbers, i.e., for high nutrient consumption rates relative to nutrient provision, nutrient supply becomes the limiting factor. Figure 6 shows (c) Da_i and (d) Da_e numbers as a function of biofilm accumulation. These figures indicate that both definitions of Da increase substantially with time for all simulation conditions consistent with a system that is increasingly mass transfer limited.

Sample Results and Biomass Accumulation Rates—With Biofilm Detachment

Figure 7 illustrated how the mean shear stress on the biofilm surface evolves as a function of biomass accumulation

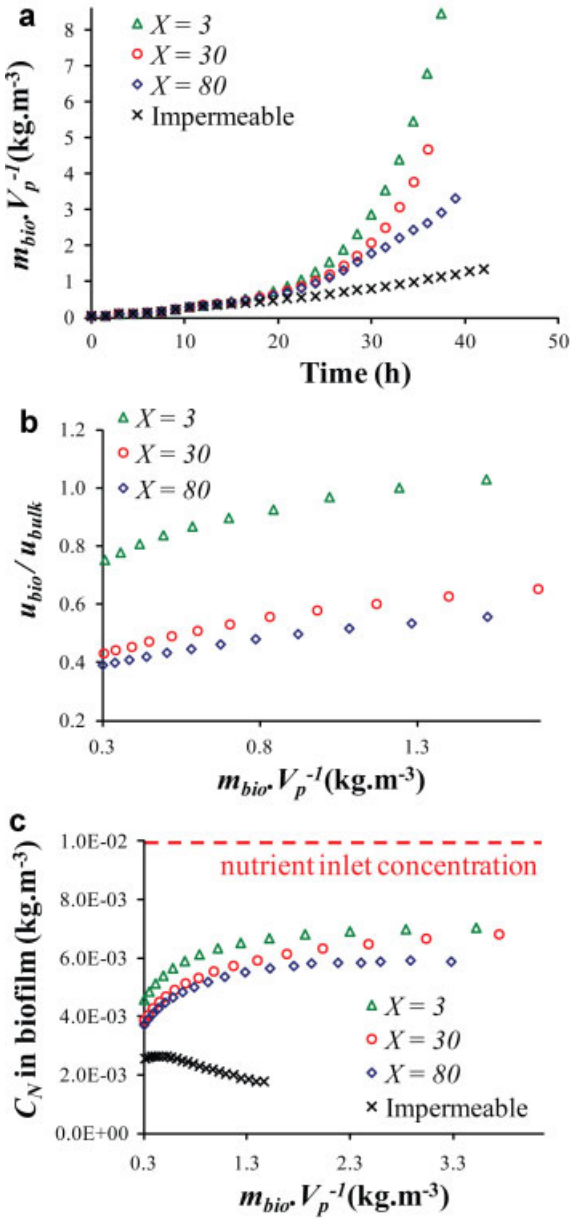

Figure 5. **a**: Temporal evolution of $m_{bio}.V_p^{-1}$ (**b**): Ratio between mean liquid velocity in the biofilm, u_{bio}, and mean bulk liquid velocity, u_{bulk}, as a function of biofilm accumulation (**c**): Average nutrient concentration in the biofilm, C_N, as a function of biomass accumulation. [Color figure can be seen in the online version of this article, available at http://wileyonlinelibrary.com/bit]

during the course of the various simulations conducted. The influence of biofilm permeability is quite distinct. Figure 8 shows slice $z = 600$ μm after 27 h of biofouling (corresponding thus to Figs. 3 and 4) when shear induced biomass detachment is included in the simulation. Two biofilms of different cohesive strength were considered, respectively, resulting in average erosion velocities per unit shear, $u_{e,w}$, of (a) 1.7×10^{-9} (strong biofilm) and (b) 3.5×10^{-9} m.s^{-1}.Pa^{-1} (weak biofilm), respectively. It is clear that the comparatively weaker biofilm exhibits minimal biomass accumulation (Fig. 8(b)) for all biofilm permeabilities considered. With respect to the comparatively stronger biofilm (Fig. 8(a)), biomass accumulation is clearly still a strong function of biofilm permeability.

In Figure 9 we show the biomass accumulation as a function of time for all biofilm permeabilities for this comparatively stronger biofilm. Whilst overall biomass accumulation is significantly reduced compared to Figure 5(a), the dependency on biofilm permeability is consistent. After 40 h of biofilm accumulation, for a biofilm permeability of 1/80 of that of the free space presents a comparative increase in biomass by a factor of 3.05 is observed; the equivalent number in the absence of biomass detachment was 3.08.

Influence of Biofilm Permeability on Overall Porous Medium Conductivity

The overall conductivity of the simulation cell (Fig. 2), κ, was determined given the imposed volumetric flowrate, the simulation determined pressure drop and Darcy's law (as presented in Equation 2). Figure 10 shows how this overall conductivity varies as a function of time (normalized by the initial permeability of the completely unfouled simulation cell). What is immediately obvious is overall conductivity reduction (due to biomass accumulation) is a weak function of biofilm permeability when there is significant difference in permeability between free pore space and that in the biofilm regions.

Conclusions

We have successfully incorporated biofilm permeability into a biofilm growth model compatible with porous media support structures. This revealed the importance of biofilm permeability in determining biomass accumulation rates when sufficient biomass accumulation had occurred to enact mass transfer limitations in nutrient provision. This effect was retained when biomass detachment was included in the model. Inclusion of biofilm permeability is likely to be very relevant to simulations of bio-clogging events, such as is the case in bio-barrier scenarios which feature significant biomass accumulation in order to reduce system hydraulic conductivity. Biofilm permeability can probably be safely ignored in scenarios when thin biofilms develop and mass transfer-limitations are minimal.

Whilst our modeling study has identified the importance of (even) very low biofilm permeabilities on biomass accumulation, clearly there are a number of necessary assumptions in its formulation that make it more suitable for trend predictions (as was the focus of the current work) as opposed to exact scenario prediction. Certainly we consider that future efforts should focus on experimentally quantifying the relationship between local biofilm

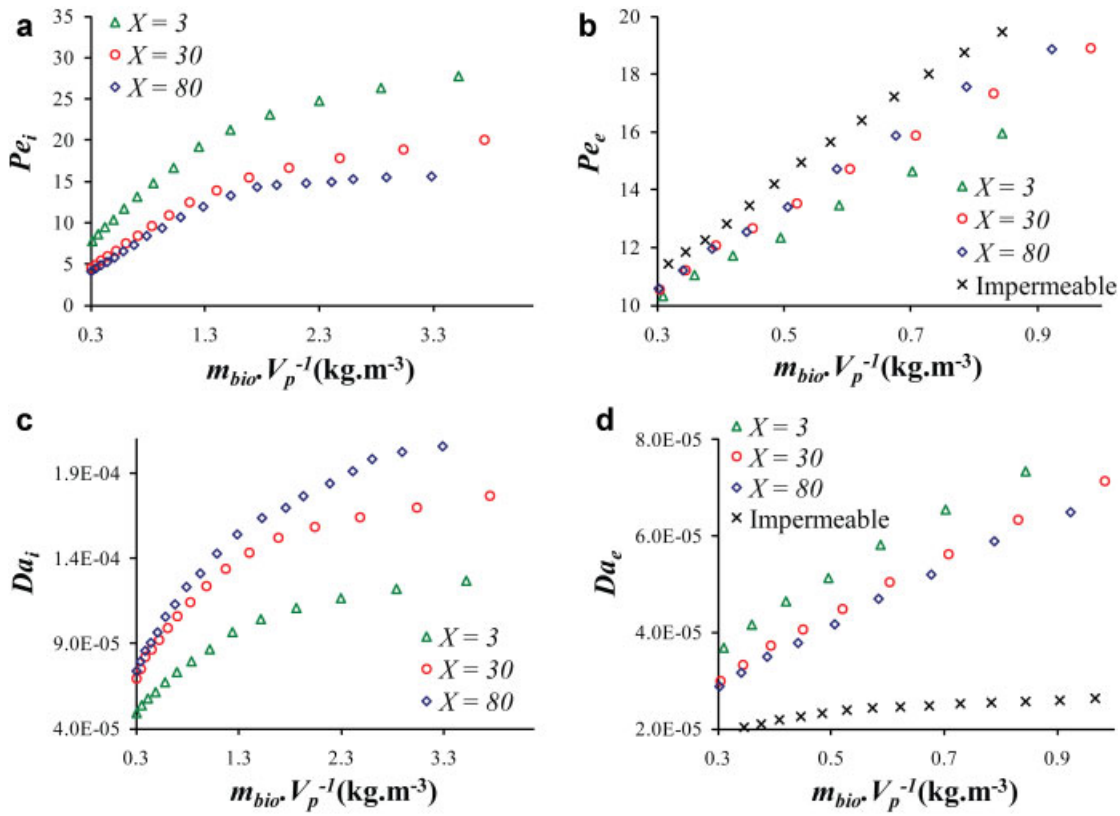

Figure 6. **a**: Pe_i, (**b**) Pe_e, (**c**) Da_i, and (**d**) Da_e as a function of biomass accumulation. [Color figure can be seen in the online version of this article, available at http://wileyonlinelibrary.com/bit]

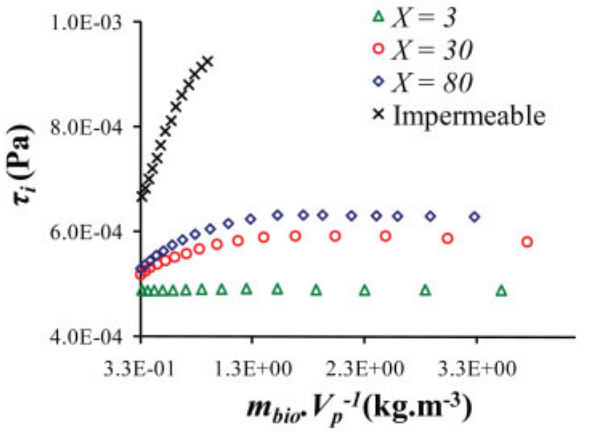

Figure 7. Average shear stress, τ_i, at the interface between biofilm and bulk liquid for an impermeable biofilm and permeable biofilms with $X = 3$, 30, and 80. [Color figure can be seen in the online version of this article, available at http://wileyonlinelibrary.com/bit]

microstructure and permeability, hence enabling a physical and local value for X to be included in our model. This is being attempted using magnetic resonance velocity (MRV) measurements through biofilm structures grown on various support structures; however, it is a very challenging exercise due to the inhomogeneity of the biofilm structure and more importantly the difficulty in simultaneously detecting flow in the biofilm structures that is orders of magnitude lower than that in the free pore space. MRV and its imaging equivalent, MRI, will however present fairly course spatial resolution. With respect to imaging heterogeneous biofilm microstructures we note the recent progress in the use of X-ray Microtomography (XMT) in terms of providing high resolution 3D images of biofilm microstructure in complex systems (Davit et al., 2011; Iltis et al., 2011). Collectively such data could provide quantitative experimental evidence of biofilm permeability, provide the required relationship between local biofilm permeability and microstructure and also provide excellent simulation lattices for model validation.

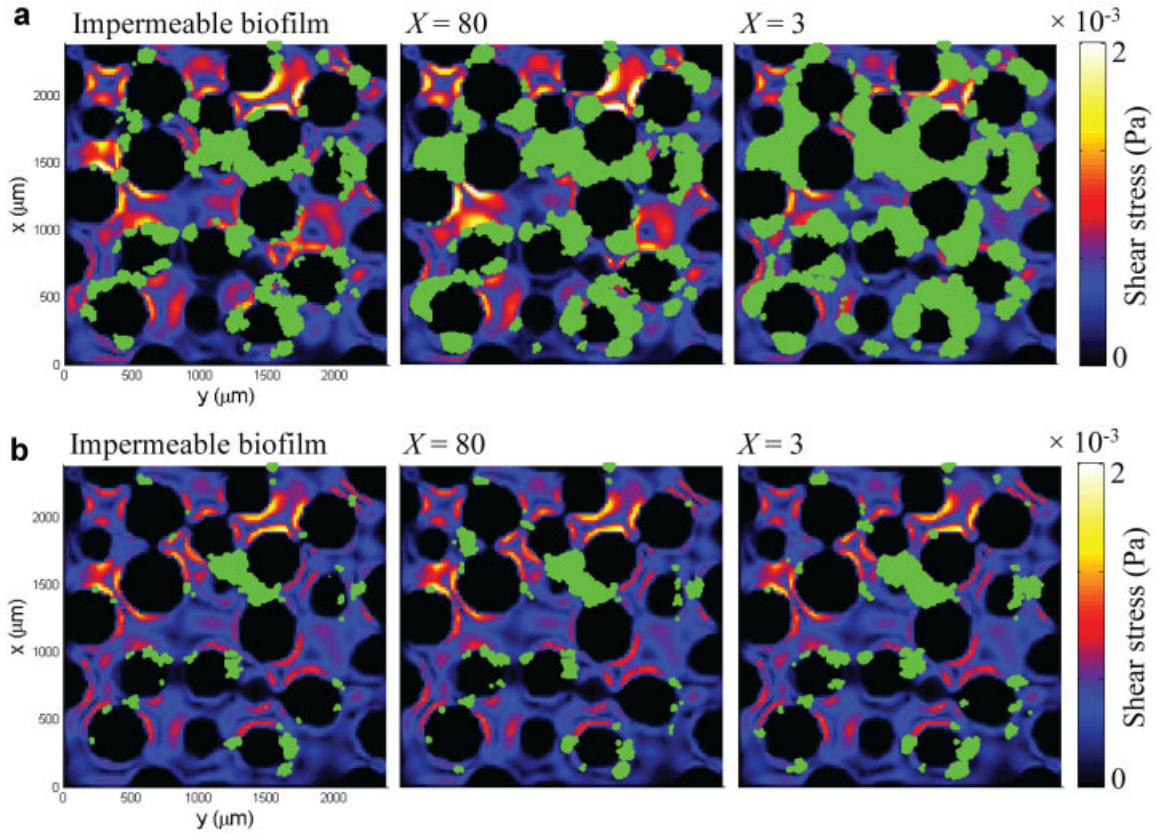

Figure 8. Shear stress fields and biofouling extent (shown in green) at slice $z = 600\,\mu m$ (of a full 4D data set) after 27 h of biofilm growth for an impermeable biofilm and permeable biofilms with $X = 80$ and $X = 3$. Biomass was allowed to detach depending on adjacent shear stresses with average erosion velocities per unit shear stress, $u_{e,w}$, of (**a**) 1.7×10^{-9} (comparatively strong biofilm) and (**b**) 3.5×10^{-9} m.s^{-1}.Pa^{-1} (comparatively weak biofilm). The suprficial flow direction (z) is pointed inwards to the plane. [Color figure can be seen in the online version of this article, available at http://wileyonlinelibrary.com/bit]

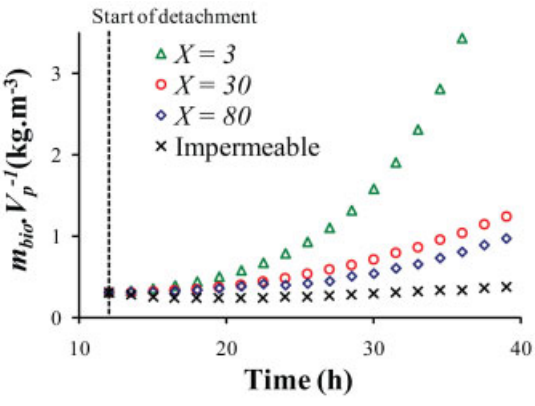

Figure 9. Temporal evolution of biofilm accumulation in the porous medium for biofilms of different permeability and average erosion velocities per unit shear stress, $u_{e,w}$, of 1.7×10^{-9} m.s^{-1}.Pa^{-1}. [Color figure can be seen in the online version of this article, available at http://wileyonlinelibrary.com/bit]

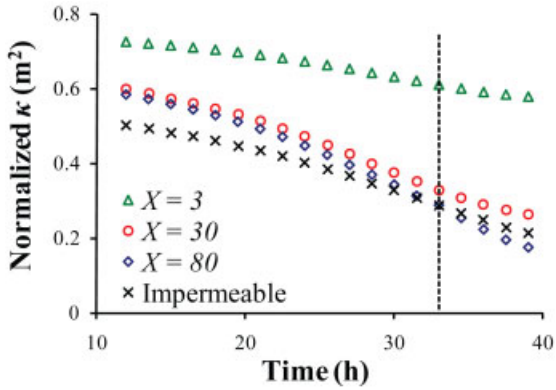

Figure 10. Normalized overall system hydraulic conductivity permeability versus time. [Color figure can be seen in the online version of this article, available at http://wileyonlinelibrary.com/bit]

This research was supported by the Engineering and Physical Sciences Research Council (EPSRC—EP/E012205/1), Selwyn College, and the Cambridge Commonwealth Trust.

References

Alpkvist E, Klapper I. 2007. Description of mechanical response including detachment using a novel particle model of biofilm/flow interaction. Water Sci Technol 55(8–9):265–273.

Beeftink HH, van der Heijden RTJM, Heijnen JJ. 1990. Maintenance requirements: Energy supply from simultaneous endogenous respiration and substrate consumption. FEMS Microb Ecol 73:203–209.

Bijeljic B, Muggeridge AH, Blunt MJ. 2004. Pore-scale modeling of longitudinal dispersion. Water Resour Res 40(11):W11501.

Clement TP, Peyton BM, Skeen RS, Jennings DA, Petersen JN. 1997. Microbial growth and transport in porous media under denitrification conditions: Experiments and simulations. J Contam Hydrol 24(3–4): 269–285.

Cunningham AB, Sharp RR, Hiebert R, James G. 2003. Subsurface biofilm barriers for the containment and remediation of contaminated groundwater. Bioremed J 7(3–4):151–164.

d'Humières D, Ginzburg I, Krafczyk M, Lallem P, Luo LS. 2002. Multiple-relaxation-time lattice Boltzmann models in three dimensions. Phil Trans Roy Soc Lond Math Phys Sci 360(1792):437–451.

Davit Y, Ilsit G, Debenest G, Veran-Tissoires S, Wildenschield D, Gerino M, Quintard M. 2011. Imaging biofilm in porous media using X-ray computed microtomography. J Microsc 242(1):15–25.

Dupin HJ, Kitanidis PK, McCarty PL. 2001a. Pore-scale modeling of biological clogging due to aggregate expansion: A material mechanics approach. Water Resour Res 37(12):2965–2979.

Dupin HJ, Kitanidis PK, McCarty PL. 2001b. Simulations of two-dimensional modeling of biomass aggregate growth in network models. Water Resour Res 37(12):2981–2994.

Flekkøy EG. 1993. Lattice Bhatnagar-Gross-Krook models for miscible fluids. Phys Rev E 47(6):4247–4257.

Flemming HC, Szewzyk U, Griebe T. 2000. Biofilms: Investigative methods & applications, (Chapter 1). Lancaster, PA: Technomic Publishing Co.

Flemming HC, Wingender J. 2002. What biofilms contain - Proteins, polysaccharides, etc. Chem Unserer Zeit 36(1):30–42.

Freund H, Zeiser T, Huber F, Klemm E, Brenner G, Durst F, Emig G. 2003. Numerical simulations of single phase reacting flows in randomly packed fixed-bed reactors and experimental validation. Chem Engin Sci 58(3–6):903–910.

Fuqua WC, Winans SC, Greenberg EP. 1994. Quorum sensing in bacteria: The LuxR-LuxI family of cell density- responsive transcriptional regulators. J Bacteriol 176(2):269–275.

Gikas P, Livingston AG. 1997. Specific ATP and specific oxygen uptake rate in immobilized cell aggregates: Experimental results and theoretical analysis using a structured model of immobilized cell growth. Biotechnol Bioeng 55(4):660–673.

Graf von der SchulenburgDA, Pintelon TRR, Picioreanu C, Van Loosdrecht MCM, Johns ML. 2009. Three-dimensional simulations of biofilm growth in porous media. AIChE J 55(2):494–504.

Hu ZQ, Ferraina RA, Ericson JF, MacKay AA, Smets BF. 2005. Biomass characteristics in three sequencing batch reactors treating a wastewater containing synthetic organic chemicals. Water Res 39(4):710–720.

Iltis GC, Armstrong RT, Jansik DP, Wood BD, Wildenschild D. 2011. Imaging biofilm architecture within porous media using synchrotron-based X-ray computed microtomography, Water Resour Res 47: W02601.

Kao CM, Chen SC, Liu JK. 2001. Development of a biobarrier for the remediation of PCE-contaminated aquifer. Chemosphere 43(8):1071–1078.

Kapellos GE, Alexiou TS, Payatakes AC. 2007. Hierarchical simulator of biofilm growth and dynamics in granular porous materials. Adv Water Resour 30(6–7):1648–1667.

Klapper I, Rupp CJ, Cargo R, Puvedorj B, Stoodley P. 2002. Viscoelastic fluid description of bacterial biofilm material properties. Biotechnol Bioeng 80(3):289–296.

Kim DS, Fogler HS. 2000. Biomass evolution in porous media and its effects on permeability under starvation conditions. Biotechnol Bioeng 69(1):47–56.

Kim G, Lee S, Kim Y. 2006. Subsurface biobarrier formation by microorganism injection for contaminant plume control. J Biosci Bioeng 101(2):142–148.

Komlos J, Cunningham AB, Camper AK, Sharp RR. 2004. Biofilm barriers to contain and degrade dissolved trichloroethylene. Environ Progr 23(1):69–77.

Kreft JU, Booth G, Wimpenny JWT. 1998. BacSim, a simulator for individual-based modelling of bacterial colony growth. Microbiology-Uk 144:3275–3287.

Lallemand P, Luo LS. 2000. Theory of the lattice Boltzmann method: Dispersion, dissipation, isotropy, Galilean invariance, and stability. Phys Rev E 61(6):6546–6562.

Lappin-Scott HM, Costerton JW. 2003. Microbial biofilms. Cambridge: Cambridge University Press.

Macleod FA, Lappinscott HM, Costerton JW. 1988. Plugging of a model rock system by using starved bacteria. Appl Environ Microbiol 54(6): 1365–1372.

Maier RS, Kroll DM, Kutsovsky YE, Davis HT, Bernard RS. 1998. Simulation of flow through bead packs using the lattice Boltzmann method. Phys Fluids 10:60–74.

Manz B, Gladden LF, Warren PB. 1999. Flow and dispersion in porous media: Lattice-Boltzmann and NMR studies. AIChE J 45:1845–1854.

Olivera-Nappa A, Picioreanu C, Asenjo JA. 2010. Non-homogeneous biofilm modelling applied to bioleaching process. Biotechnol Bioeng 106(4):660–676.

Park JS, Lee CH. 2005. Removal of soluble COD by a biofilm formed on a membrane in a jet loop type membrane bioreactor. Water Res 39(19): 4609–4622.

Picioreanu C, van Loosdrecht MCM, Heijnen JJ. 2000. Effect of diffusive and convective substrate transport on biofilm structure formation: A two-dimensional modeling study. Biotechnol Bioeng 69(5):504–515.

Pintelon TRR, Creber SA, Graf vonder, Schulenburg DA, Johns ML. 2010. Validation of 3D simulations of reverse osmosis membrane biofouling. Biotechnol Bioeng 106(4):677–689.

Pintelon TRR, von der Schulenburg DAG, Johns ML. 2009. Towards optimum permeability reduction in porous media using biofilm growth simulations. Biotechnol Bioeng 103(4):767–779.

Pratt LA, Kolter R. 1998. Genetic analysis of Escherichia coli biofilm formation: Roles of flagella, motility, chemotaxis and type I pili. Mol Microbiol 30(2):285–293.

Raabe D. 2004. Overview of the lattice Boltzmann method for nano- and microscale fluid dynamics in materials science and engineering. Model Simul Mater Sci 12:13–46.

Radu AI, Vrouwenvelder JS, van Loosdrecht MCM, Picioreanu C. 2010. Modeling the effect of biofilm formation on reverse osmosis performance: Flux, feed channel pressure drop and solute passage. J Membr Sci 365(1–2):1–15.

Sahraoui M, Kaviany M. 1994. Slip and no-slip temperature boundary conditions at the interface of porous, plain media: Convection. Int J Heat Mass Transf 37(6):1029–1044.

Shaw JC, Bramhill B, Wardlaw NC, Costerton JW. 1985. Bacterial fouling in a model core system. Appl Environ Microbiol 49(3):693–701.

Stewart PS, Costerton JW. 2001. Antibiotic resistance of bacteria in biofilms. Lancet 358(9276):135–138.

Sullivan SP, Gladden LF, Johns ML. 2006. 3D chemical reactor LB simulations. Math Comput Simulat 72(2–6):206–211.

Taylor JP, Wilson B, Mills MS, Burns RG. 2002. Comparison of microbial numbers and enzymatic activities in surface soils and subsoils using various techniques. Soil Biol Biochem 34(3):387–401.

Thullner M, Baveye P. 2008. Computational pore network modeling of the influence of biofilm permeability on bioclogging in porous media. Biotechnol Bioeng 99(6):1337–1351.

Thullner M, Zeyer J, Kinzelbach W. 2002. Influence of microbial growth on hydraulic properties of pore networks. Transport Porous Media 49(1): 99–122.

Vandevivere P, Baveye P. 1992. Saturated hydraulic conductivity reduction caused by aerobic-bacteria in sand columns. Soil Sci Soc Am J 56(1): 1–13.

Wanner O, Eberl HJ, Morgenroth E, Noguera D, Picioreanu C, Rittmann BE, van Loosdrecht MCM. 2006. Mathematical modeling of biofilms. IWA scientific and technical report 710 No.18. London, UK: IWA Publishing.

Weiss RF. 1970. Solubility of nitrogen, oxygen and argon in water and seawater. Deep Sea Res 17(4):721–735.

Zeiser T, Lammers P, Klemm E, Li YW, Bernsdorf J, Brenner G. 2001. CFD-calculation of flow, dispersion and reaction in a catalyst filled tube by the lattice Boltzmann method. Chem Eng Sci 56(4):1697–1704.